Beryllium and Indium Activation Measurements of Total Neutron Yield from a Pulsed Photoneutron Source

Introduction

A pulsed photoneutron source consisting of a beryllium sphere and a 5 MeV endpoint 30 ns bremsstrahlung beam emanating from the Mercury pulsed-power source was assembled and tested in October 2017 at the Naval Research Lab (NRL) in Washington, D.C. [1]. Among the diagnostics used to characterize the source were indium and beryllium activation detectors that measured the total neutron yield in each pulse. The indium activation detectors were calibrated in December 2017 at the University of Missouri Research Reactor (MURR) to determine detector response to a known neutron flux using the F-factor method. These detectors were highly sensitive, mechanically robust, and resistant to the high-RF noise environment inside the facility.

The indium detectors were placed in different positions around the source to estimate the scatter background and to compare the yield of smaller beryllium targets and empty shots. Detectors that were placed below the source on top of a steel table showed a mean yield of 1.046±0.022E10 neutrons, while detectors in the plane of the source measured yields of 6.45±0.34E09 or 5.81±0.21E09 neutrons depending on orientation within the plane. Detectors placed above the source measured a yield of only 3.81±0.15E09 neutrons, indicating that the scatter background accounts for a large portion of the neutrons detected near the table. Self-shielding by the beryllium sphere was observed because the yield measured when only the core of the sphere was used was 3.07±0.24E09 neutrons, and the outer shell 2.42±0.33E09 neutrons. The sum of the yields of constituent components is larger than the yield of the full sphere, which measured

3.81±0.15E09 neutrons. Shot-to-shot variation was estimated to be 20%, based on thermal-neutron-insensitive beryllium detector data.

Theory

Activation detectors are small samples of material that are activated into excited states by impinging neutrons; the subsequent decay is measured with a secondary detector. For this experiment, indium pucks were used to take advantage of $^{115}\text{In}(n,n')^{115m}\text{In}$ elastic scattering with a threshold energy of approximately 340 keV and a 4.5 hour half-life and $^{115}\text{In}(n,\gamma)^{116m}\text{In}$ neutron capture with a 54 minute half-life and a large cross section even at thermal energies (figure 1) [2]. The metastable indium states ^{115m}In and ^{116m}In then decay according to the decay schemes shown in figure 2, emitting characteristic gamma rays that were then measured using an ORTEC high-purity germanium (HPGe) handheld radioisotope identifier [2]. The beryllium rod detector was configured similarly to the indium activation detectors, and the beryllium samples were read out using a photomultiplier tube and ORTEC Easy MCS multichannel scaler rather than an HPGe detector. The reaction being used was $^{9}\text{Be}(n,\alpha)^{6}\text{He}$ (threshold of 667 keV) and required immediate measurement due to its 0.8 s half-life.

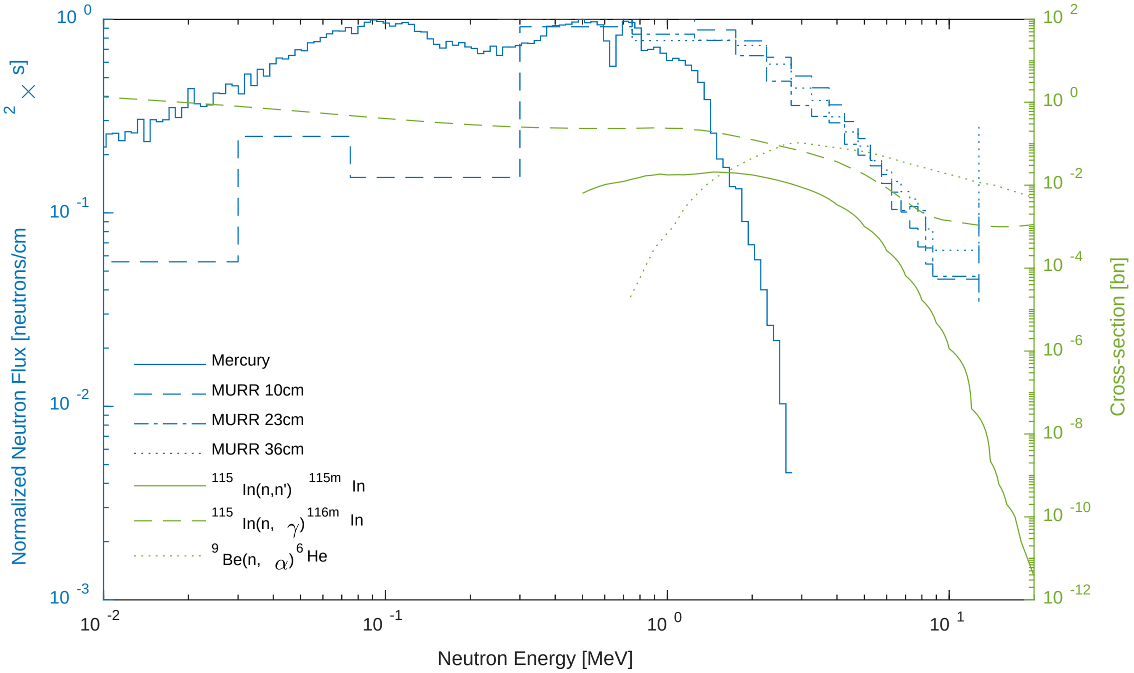

Figure 1: Source spectra used in this experiment are displayed in blue. Neutron capture; elastic scattering cross sections of indium and beryllium as a function of neutron energy are displayed in green.

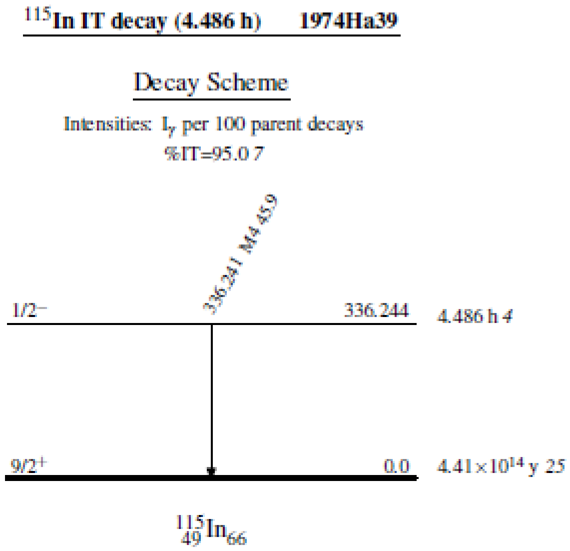

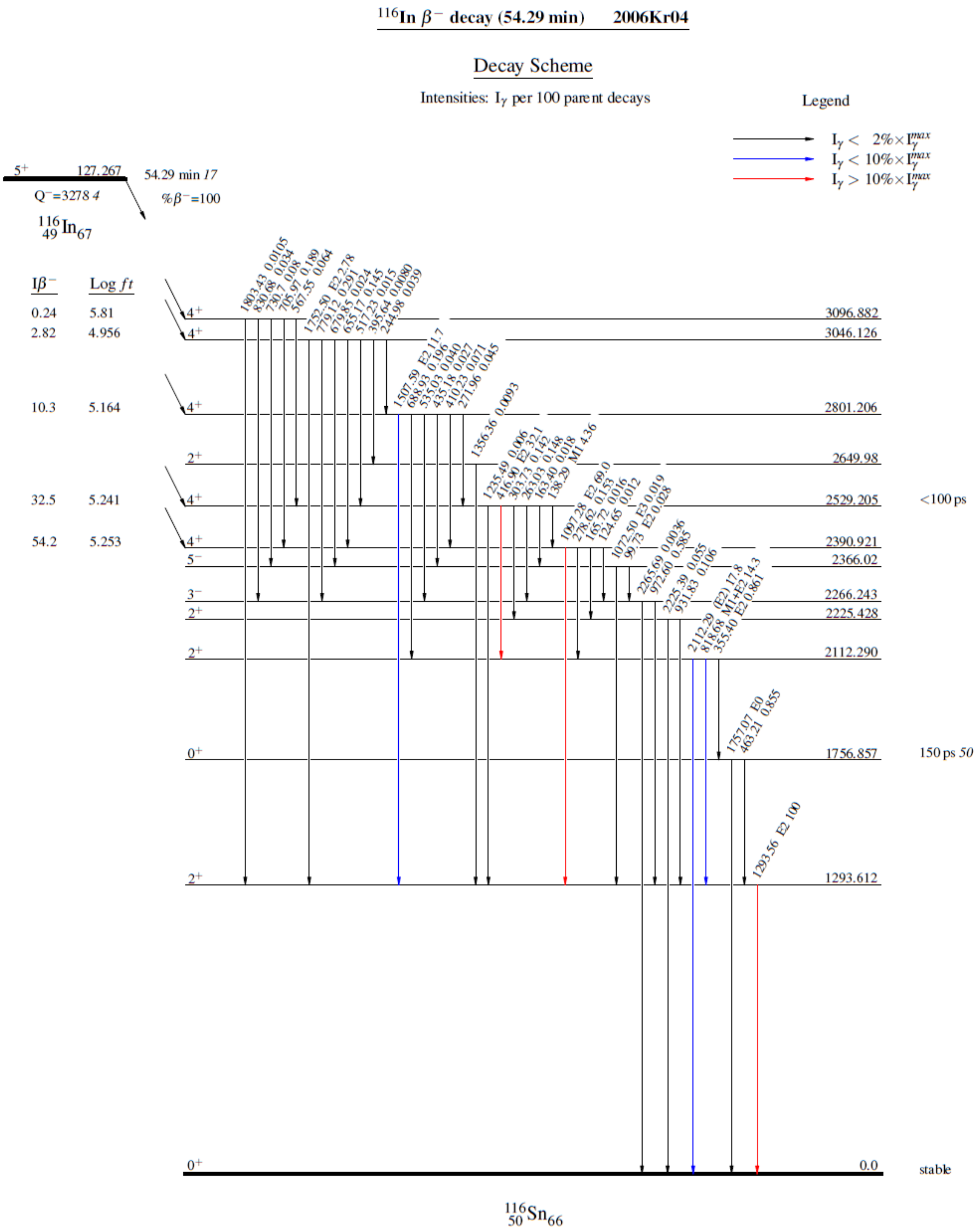

Figure 2: Decay schemes of ^{115m}In and ^{116m}In. There is only one characteristic gamma ray emitted by the internal transition in ^{115m}In, while there are many in the beta decay of

^{116m}In. The gamma rays with intensities of greater than 10% per ^{116m}In parent decay are displayed in red and blue; these were the gamma rays measured in this experiment.

The total neutron yield can be calculated from the area under the gamma ray peaks in the HPGe detector if the system response is measured under a known neutron flux. This method, known as the F-factor, has the advantage of including detector efficiencies, cross sections, and self-absorption in the calibration without detailed knowledge of the system [4,5]. The F-factor is a proportionality constant that relates the total neutron yield to known quantities of distance from the source, sample mass, net counts under a peak in the HPGe spectrum, and start and stop times after the neutron pulse strikes the sample. The following derivation closely tracks Cooper and Knoll [4,6].

The process begins by identifying the number of metastable nuclides, $N(t)$, formed when a sample is exposed to a neutron flux. Here, R is the reaction rate of the nuclide, t is the irradiation time, and λ is the decay constant of the nuclide.

$$N(t) = \frac{R\left(1-e^{-\lambda t}\right)}{\lambda} \qquad (1)$$

The reaction rate, in turn, is related to the neutron flux φ by factors of the abundance of the isotope of interest ε_A, sample mass M, Avogadro's number N_{Av}, the neutron capture cross section $\sigma(E)$, and inversely related to the atomic weight A_W.

$$R = \varphi \varepsilon_A M N_A \sigma(E)/A_W \qquad (2)$$

The total number of nuclides created after irradiation for a time t_0 is then given by

$$N(t_0) = \frac{\varphi \varepsilon_A M N_A \sigma(E)\left(1-e^{-\lambda t_0}\right)}{\lambda A_W}. \qquad (3)$$

When the metastable states decay, they will produce gamma rays at a rate $dN/dt = -\lambda N$. Integrating over the readout time from t_1 to t_2 after irradiation will give the total number of gammas emitted within the counting period. Multiplying by the detector efficiency ε_D, self-absorption factor ε_S, and branching ratio ε_B, the net counts (counts minus background, or $C - B$) under the peak are related to the total number of nuclides by eq. 4.

$$C - B = \varphi\varepsilon_A\varepsilon_D\varepsilon_S\varepsilon_B\ MN_A\sigma(E)\left(1 - e^{-\lambda t_0}\right)\left(e^{-\lambda t_1} - e^{-\lambda t_2}\right)/\lambda A_W \quad (4)$$

The neutron flux from an isotropic point source into the indium puck is equal to the total yield Y divided by irradiation time and the surface area of a sphere at the distance of the puck (d),

$$\varphi = \frac{Y}{4\pi d^2 t_0}\,. \quad (5)$$

Inserting the flux into eq. 4, the F-factor can be seen as the proportionality constant relating the net counts under a peak to the total yield purely in terms of experimentally determined quantities.

$$F = (C - B)t_0 4\pi d^2\lambda/YM\left(1 - e^{-\lambda t_0}\right)\left(e^{-\lambda t_1} - e^{-\lambda t_2}\right) \quad (6)$$

In terms of efficiencies, this reads as $F = \varepsilon_A\varepsilon_D\varepsilon_S\varepsilon_B\sigma(E)N_A/A_W$. Because this experiment used a 30 ns bremsstrahlung beam, the neutron pulse was sufficiently brief to allow the approximation $\lambda t_0 \approx 1 - e^{-\lambda t_0}$, so the F-factor simplifies to

$$F = (C - B)t_0 4\pi d^2\lambda/YM\left(e^{-\lambda t_1} - e^{-\lambda t_2}\right), \quad (7)$$

and the equation for the yield becomes

$$Y = (C - B)(4\pi d^2)/FM\left(e^{-\lambda t_1} - e^{-\lambda t_2}\right). \quad (8)$$

Method

A beryllium sphere of outer diameter 11.43 cm (inner diameter 2.16 cm) was positioned in front of the Mercury pulsed-power source to produce photoneutrons through the ^{9}Be(γ,n)2α reaction. The Mercury source is an inductive voltage adder configured to deposit 130 kA on a tantalum bremsstrahlung converter in 30 ns, resulting in an intense bremsstrahlung beam with an endpoint energy of approximately 5 MeV, well above the neutron binding energy of ^{9}Be at 1.67 MeV [7]. Several diagnostics were placed around the source and beam to measure beam and neutron characteristics, as shown in figure 3.

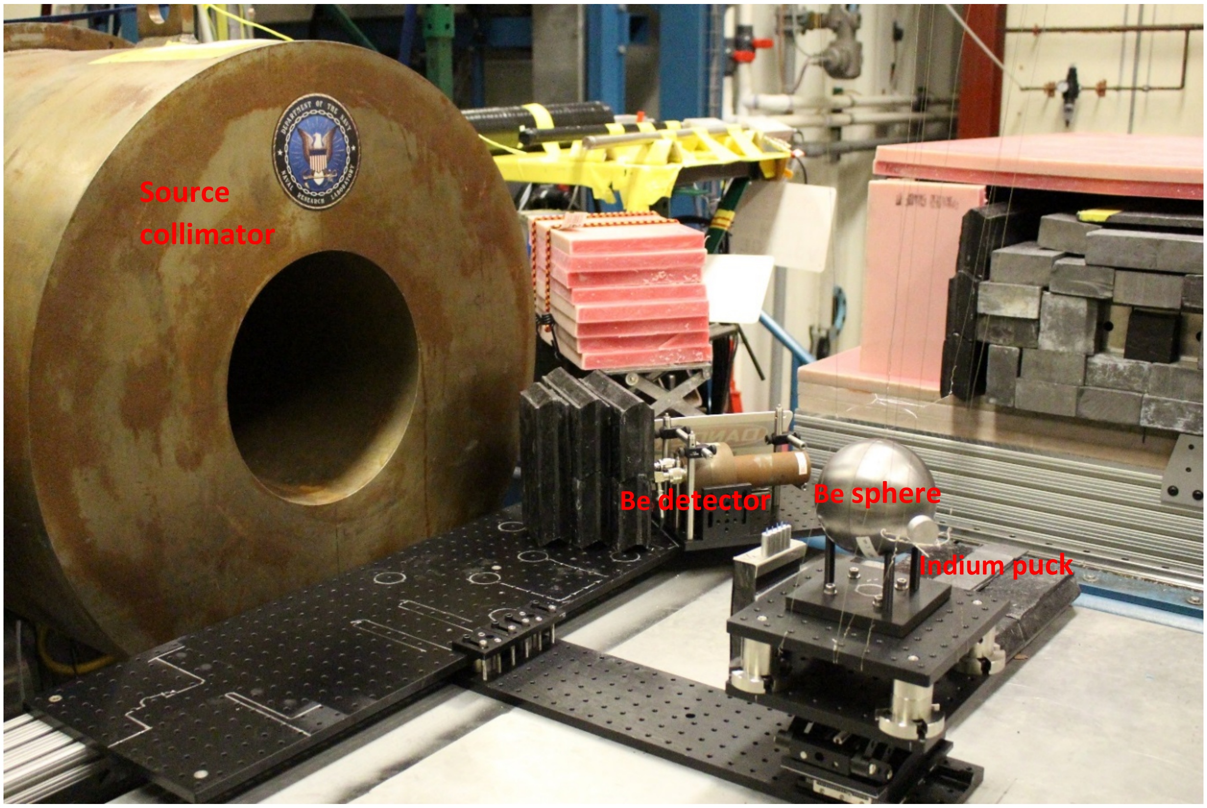

Figure 3: Mercury bremsstrahlung source collimator with beryllium sphere for photoneutron creation. Several diagnostics can be seen around the sphere, including an indium activation detector in the foreground suspended from a steel wire trapeze. The beryllium activation detector was placed away from the x-ray beam and shielded by lead to ensure it did not become a second source of neutrons.

The indium pucks were placed at several locations around the beryllium sphere, and their activity was measured after each shot using an HPGe detector. Pucks were placed on nearly massless steel wire trapezes around the sphere (see figure 4) or on top of a thin cardboard tube to minimize scattering of impinging x-rays or neutrons. Several different distances between 2 and 20 cm from the ball were sampled using one or two pucks for each shot. Different geometries were tested wherein the pucks were placed above, below, behind, beside, and 45 degrees downstream from the sphere to estimate background levels at different locations. These placements were important because other diagnostics nearby had lead or tungsten shielding that would contribute to the scatter background of the neutrons (see figure 5). A stopwatch was used to measure the time between the shot and the beginning of the HPGe readout period.

Figure 4: Indium pucks placed above and below the beryllium sphere. The indium pucks were 25 mm in diameter and 10 mm thick, while the beryllium sphere had an outer diameter of 11.3 cm.

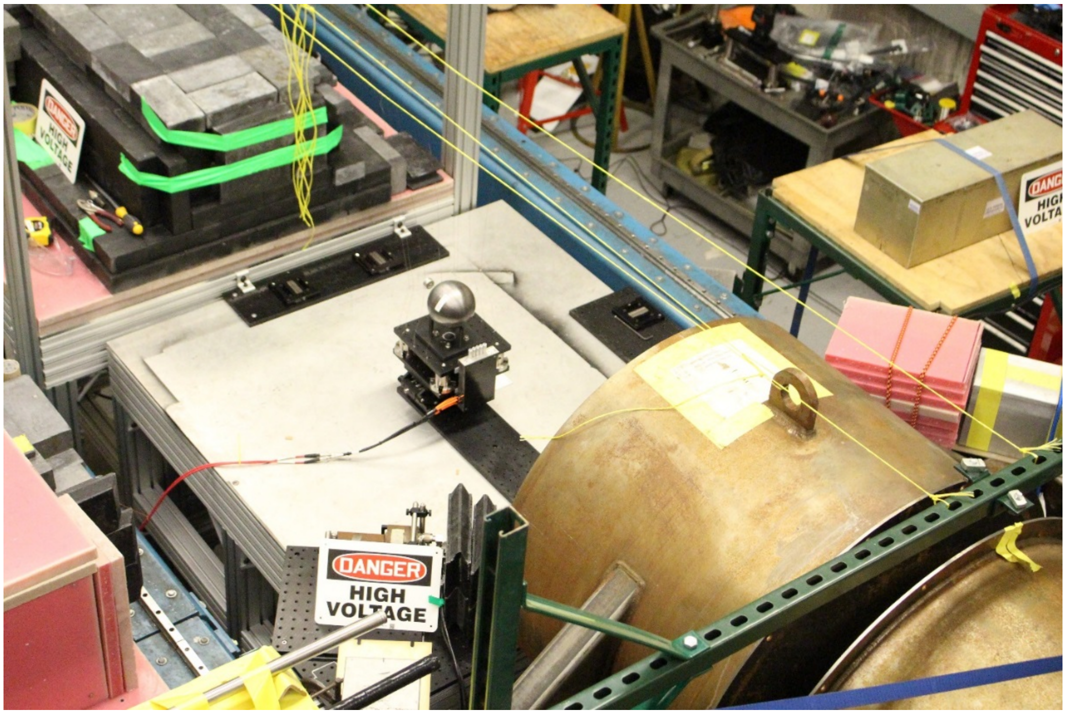

Figure 5: Diagnostics shielded with lead, tungsten, and plastic were positioned upstream, downstream, and beside the beryllium ball. The shielding contributed to the neutron scatter background of the experiment.

To obtain background measurements each day, one puck was measured without being activated. These backgrounds were indistinguishable from one another, so the pucks were presumed to be identical once ten half-lives (45 hours) had passed since activation. Empty shots were performed with no beryllium sphere but with pucks in identical positions and orientations to figure out how much signal was generated by the Mercury machine itself. This was important because the beam diameter was sufficiently large so that all of the pucks were directly exposed to x-rays as well as photoneutrons. Sample Mercury and MURR spectra are displayed in figures 6 and 7, respectively. Several shots were taken with the sphere, pucks, and beryllium rod detector in the same configuration to determine shot-to-shot variation, which was calculated to be approximately 20% using the beryllium detector.

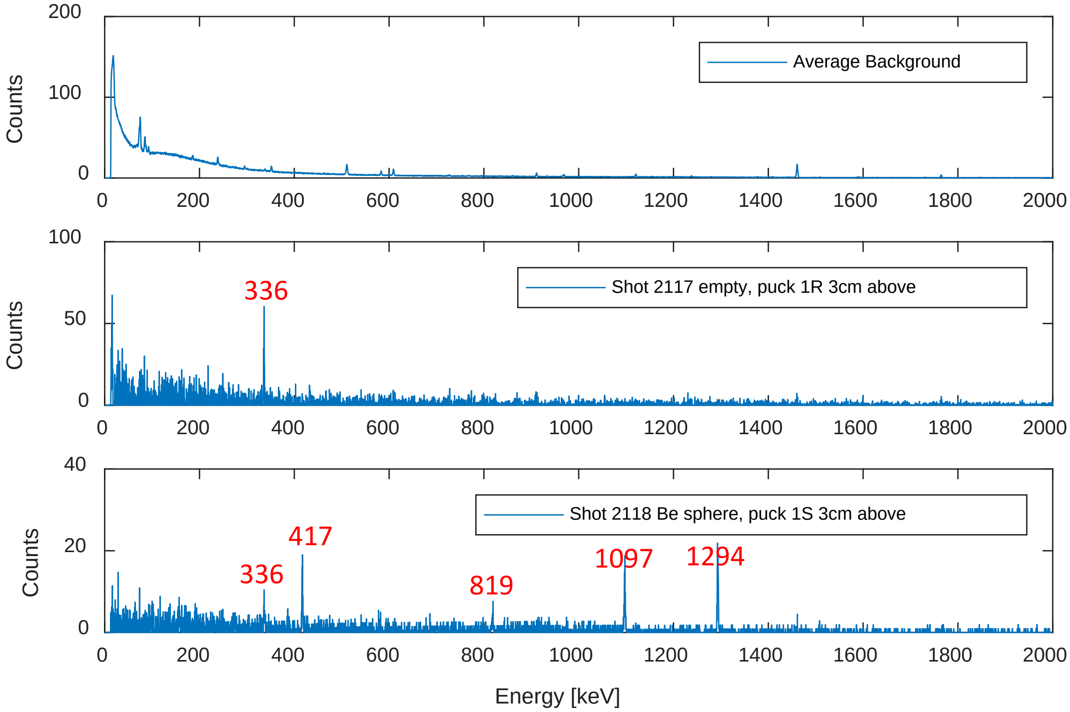

Figure 6: Sample background, empty, and beryllium sphere spectra. Activation peaks can be seen at 336, 417, 819, 1097, and 1294 keV in the beryllium sphere shot, but only the 336 keV peak (which can arise from γ,γ′ in the empty shots [8] and n,n′ in the sphere shots) is clearly visible in the empty shot. Counts are not normalized for readout time; therefore, they display higher numbers for the background and empty shots, which were integrated for long durations.

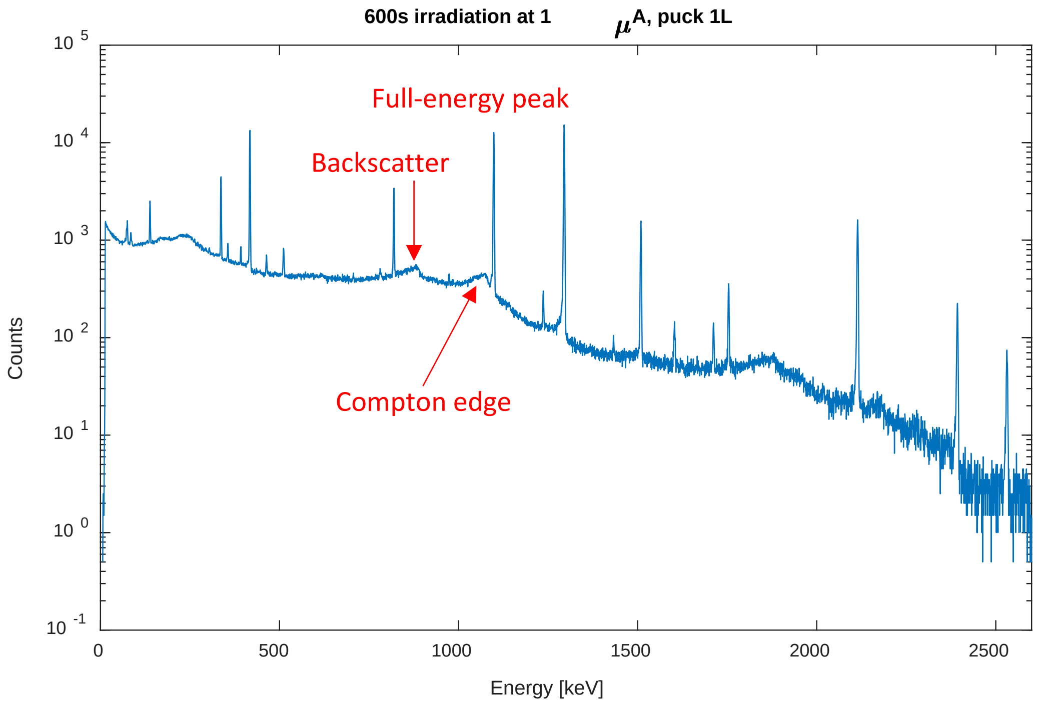

Figure 7: Binned energy spectrum at MURR; Compton edges, backscatter, annihilation peaks are visible [9].

E_g (keV)	I_g (%)
336.23	45.8
416.86	27.7
818.72	11.5
1097.33	56.2
1293.56	84.4
1507.67	10.0
2112.32	15.5

Table 1: Gamma emissions from ^{115m}In and ^{116m}In [2]

Other targets used for comparison included a bottle of D_2O, a 7.62 cm diameter aluminum sphere, and the beryllium core (inner diameter [ID] 2.16 cm, outer diameter [OD] 9.12 cm) and shell (ID 9.17 cm, OD 11.29 cm), which together constituted the beryllium sphere. Shots were made using only the shell and only the core (each containing approximately half the mass of the full sphere) to determine how much each component contributed to the total neutron yield. Readout orientation was tested to assure uniform activation of the puck—that the side of the puck facing the sphere did not yield higher counts when positioned towards the HPGe detector compared to the opposite. Lastly, signal could be detected with a long integration time 30 hours after activation, so no puck was used more frequently than once every two days.

The beryllium rod detector was configured similarly to the indium activation detectors, with the beryllium samples read out using a photomultiplier tube instead of an HPGe detector. This is due to the fact that the reaction being used was $^{9}Be(n,\alpha)^{6}He$ (threshold of 667 keV) with a half-life on only 0.8 s, requiring immediate measurement. The detector was positioned outside the x-ray beam and shielded by several inches of lead so the beryllium inside the detector did not become a source of neutrons, as shown in figure 3. The configuration was unchanged for the duration of the experiment, unlike the indium pucks, which were repositioned several times.

The method used for calibration of the indium detectors was the F-factor method detailed in [4], where the indium pucks were exposed to a known neutron flux and the detector response measured. Calibrations were performed at the Ion Beam Laboratory (IBL) in 2015 and at Missouri University Research Reactor (MURR) cyclotron in December 2017; the MURR results were used to calibrate the results for this experiment because the MURR cyclotron spectrum more closely matched the photoneutron spectrum of the experiment (see figure 1). The IBL calibration was monoenergetic at 2.45 MeV, whereas the cyclotron spectrum was broadband with a 16 MeV endpoint energy. The pucks were irradiated at the MURR cyclotron in a fixed neutron flux, and shots were taken varying current, distance, shielding, and integration time, but using the same pucks and HPGe detector so an accurate F-factor for the system could be obtained experimentally (figures 8, 9). This process allowed calibration of the entire system, including the HPGe detector, even if detailed knowledge about specific efficiencies of each part of the detection system was lacking. The scatter environment of the MURR calibration was similar to the scatter environment of the experiment (concrete walls and floor, large heavy objects such as the cyclotron magnets and lead shielding around other diagnostics), so the F-factor was not modified.

Figure 8: The MURR cyclotron (right) produced a proton beam to irradiate a 4 mL enriched water target ($^1H_2{}^{18}O$), which behaved as an isotropic point source for neutrons.

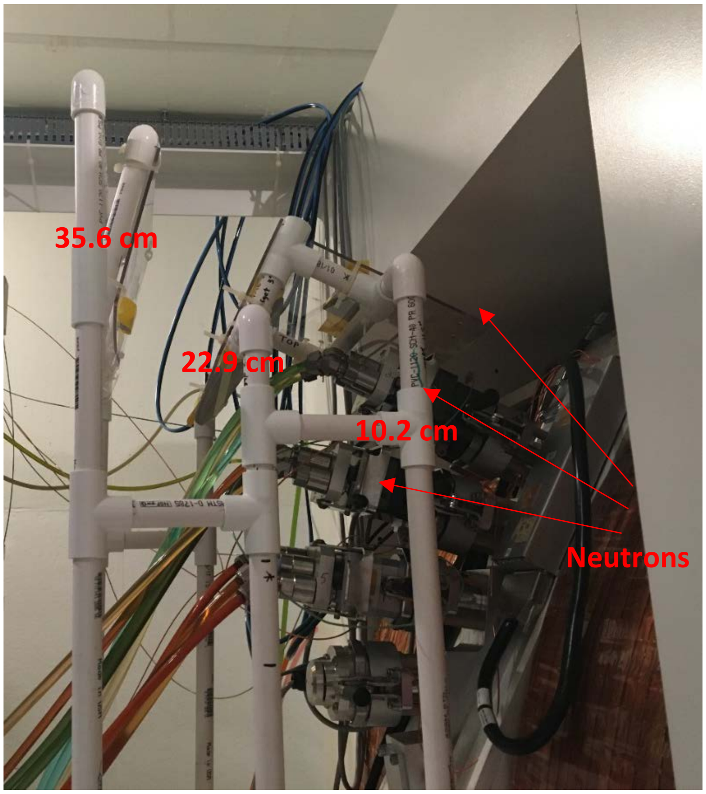

Figure 9: A PVC fixture was used for repeatable sample positioning at 10.2, 22.9, and 35.6 cm from the enriched water target. A separate sample was suspended from the ceiling out of the direct view of the target to measure the neutron scatter background in the room.

Shielding studies at MURR were performed to examine the neutron scatter. Three pucks were positioned in front of the source at different distances, and a fourth puck was positioned behind the source to measure the scatter background. Bare pucks were tested, as were pucks wrapped in cadmium and a boron-aluminum alloy. Lastly, pucks were shielded with cadmium and boron-aluminum so that they would only see the energetic parts of the spectrum directly and the full spectrum of the room return. This arrangement allowed for subtraction from the bare pucks to determine how much of the dose from the target is at thermal energies, and how much is at higher energies. As in the experiment, pucks were allowed to decay for 45 hours between activations to prevent residual activity from entering the calibration.

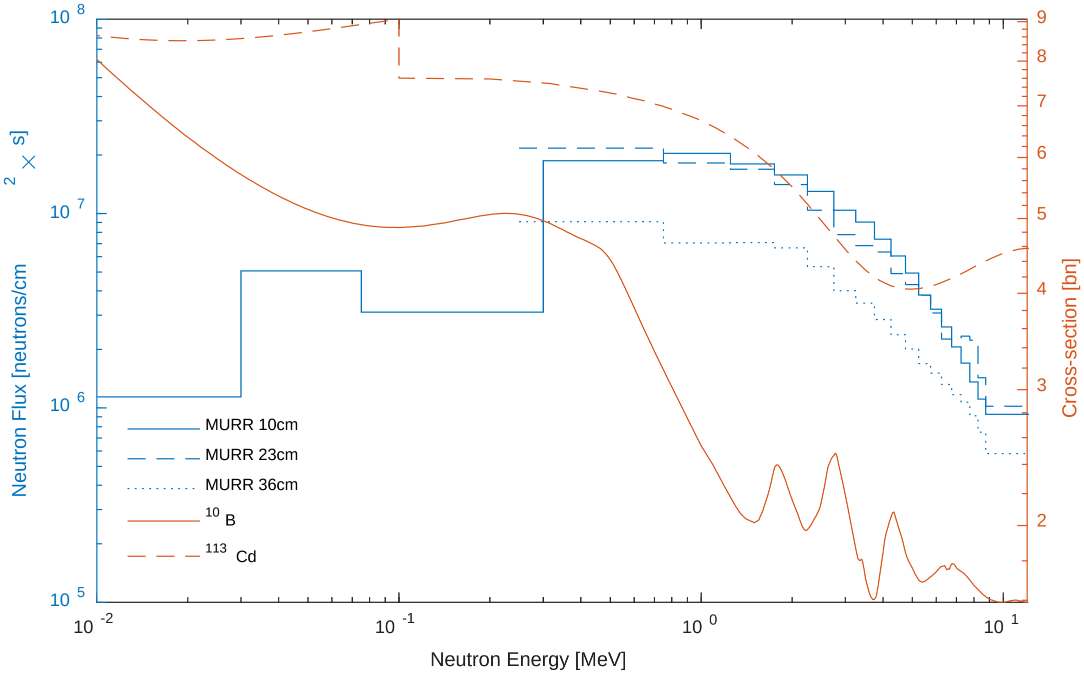

Figure 10: Neutron capture cross sections of ^{10}B and ^{113}Cd overlaid with the spectrum of the MURR cyclotron.

Results

The indium puck data from MURR and NRL were processed identically to ensure consistency. First, the data were binned in divisions of 0.65 keV, which decreased the resolution of the detector by a factor of two, for smoothing and to improve statistics. Smoothing the data came at the expense of information about the width and position of the peaks, but this was an acceptable compromise because the critical information was the total number of counts under the peak [10]. Regions of interest (ROI) for fitting were selected from the data in a ±9 keV neighborhood of each peak to ensure that the entire peak was fitted with a few points outside to average for the background.

The peaks were fitted using a skewed Gaussian and complementary error function with a locally constant background. The skewed Gaussian consisted of a Gaussian multiplied by a complementary error function, and was used to account for incomplete charge collection in the HPGe detector. The second term, another complementary error function, reflected the increased contribution of the Compton continuum in lower energies. The background was fitted by a different constant in the neighborhood of each peak. In the fitting function, A, σ, and β are, respectively, the height, width, and tail of the skewed Gaussian, B and γ are the height and width of the complimentary error function, c is the center of both the Gaussian and complimentary error function terms, and D is the constant background:

$$y = Ae^{\frac{-(x-c)^2}{\sigma^2}} erfc\left(\frac{x-c}{\beta}\right) + B\left(erfc\left(\frac{x-c}{\gamma}\right)\right) + D. \qquad (9)$$

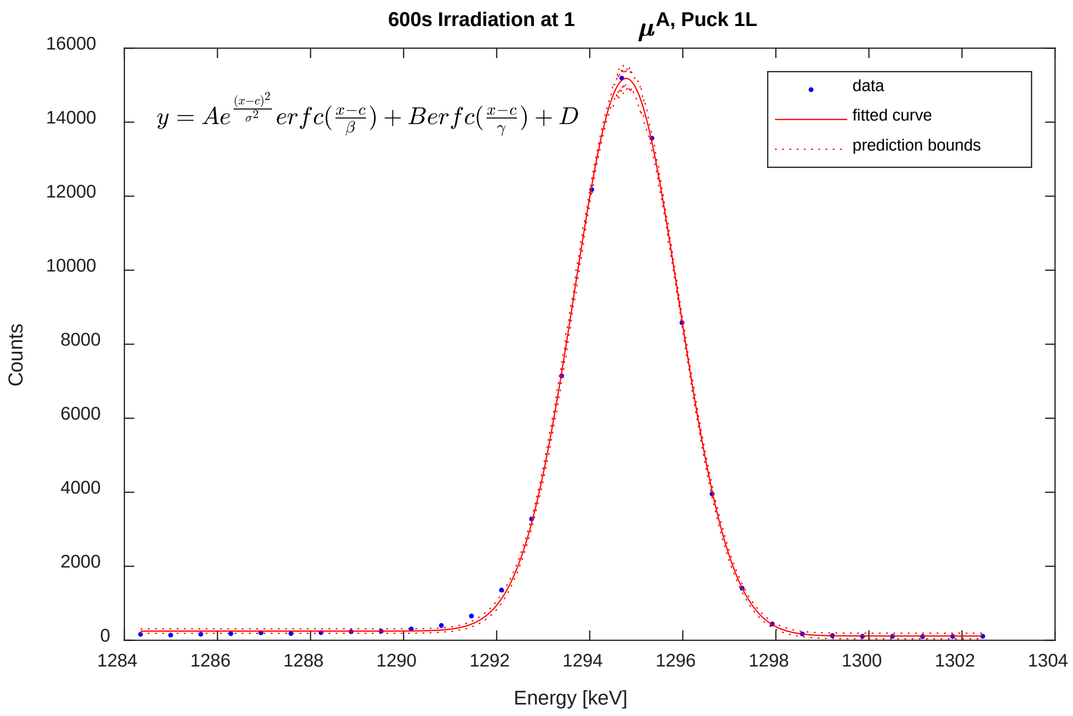

Figure 11: Fitted peak with three terms and seven free parameters. These data were used to calculate the F-factor for the 1294 keV peak, which consisted of a skewed Gaussian peak and a complementary error function on top of a locally constant background.

Physically, the peaks, widths, and backgrounds were all positive, so each fitting parameter was restricted to be at or above zero. Appropriate starting points for each of the constants were chosen so the optimization algorithm would arrive at the correct local minimum. The start point for A was the maximum value inside the ROI, c was the nominal center of the peak as stated in table 1, B and D started at the median value within the ROI, and σ, β, and γ began at 5 keV to roughly estimate the full width at half maximum of the peak. Because the rate of incomplete charge collection for each distinct peak should remain constant from measurement to measurement, B, β, and γ should be proportional to A and σ, as shown in eq. 10 below with constants c_1, c_2, and c_3:

$$y = Ae^{\frac{-(x-c)^2}{\sigma^2}} erfc\left(\frac{x-c}{c_1\sigma}\right) + C_3A\left(erfc\left(\frac{x-c}{C_2\sigma}\right)\right) + D. \qquad (10)$$

The MURR data were fitted with all seven parameters and visually checked to verify the automated algorithm made coherent results. Then, the peaks with the highest goodness-of-fit parameters (adjusted r-square > 0.99) were selected, and the quantities B/A, β/σ, and γ/σ were calculated in each fit and the median was taken. The ratios had large deviations from the median, which indicates that the quantities didn’t behave in the same manner from shot to shot. This behavior could have stemmed from an irregular background environment in the readout area caused by radiological work being done in nearby laboratories. Alternatively, it could have been caused by random instrument variations in temperature or sensitivity, or a nonlinear interdependence of parameters.

Even though the ratio B/A was unstable, it was always quite small (~0.01) for each of the peaks, so the second term was set to zero to reduce the number of fitted parameters by two at a slight cost to the fit (figure 13). The characteristic width of the Gaussian, β, was allowed to float because the ratio β/σ was not stable. This allowed the skewed part of the Gaussian to be fitted more accurately, thus improving the measurement of the area under the peak. The final fitted form of the peaks had five independent parameters and is given by:

$$y = Ae^{\frac{-(x-c)^2}{\sigma^2}} erfc\left(\frac{x-c}{\beta}\right) + D. \qquad (11)$$

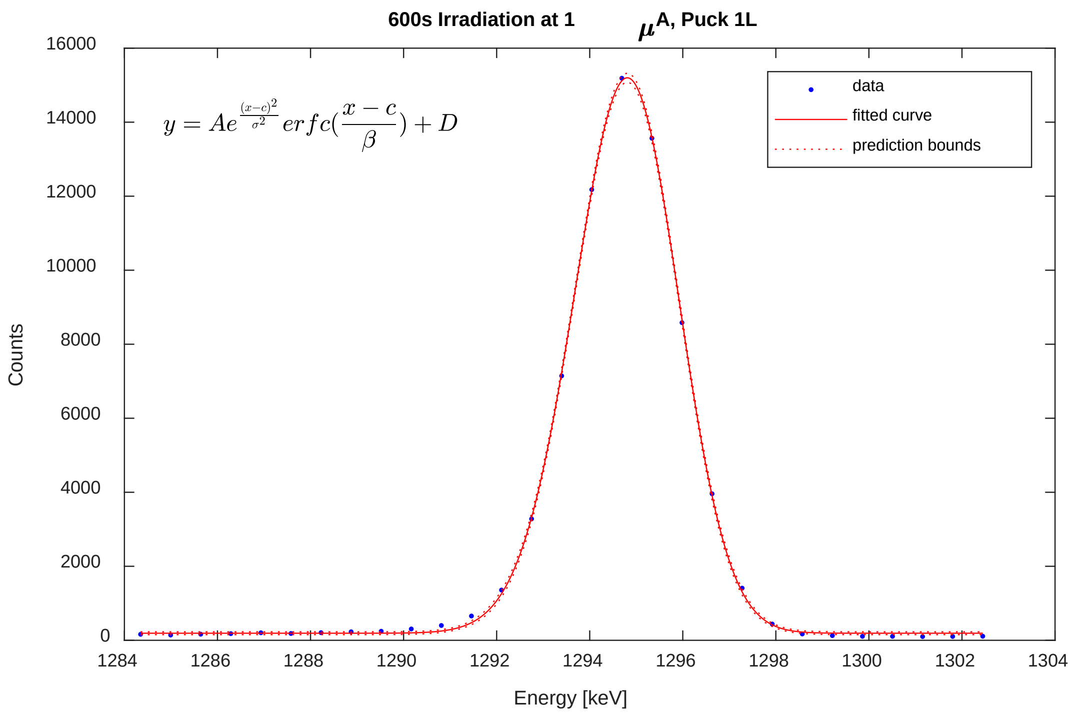

Figure 12: Fitted peak with two terms and five free parameters. This sample peak fit was used to calculate the F-factor for 1294 keV peak, which consisted of a skewed Gaussian peak on top of a locally constant background.

Contributions of each term in the fit are shown in figure 13. The seven-parameter fit more closely fits the background on both sides of the distribution, but only the amplitude of the complementary error function (B) could be constrained without degrading the fit. Because the five-parameter fit performed well with fewer free parameters, it was the final one used for determining area under each peak. The fits are displayed on a logarithmic scale to display properties of the fit components near the background level.

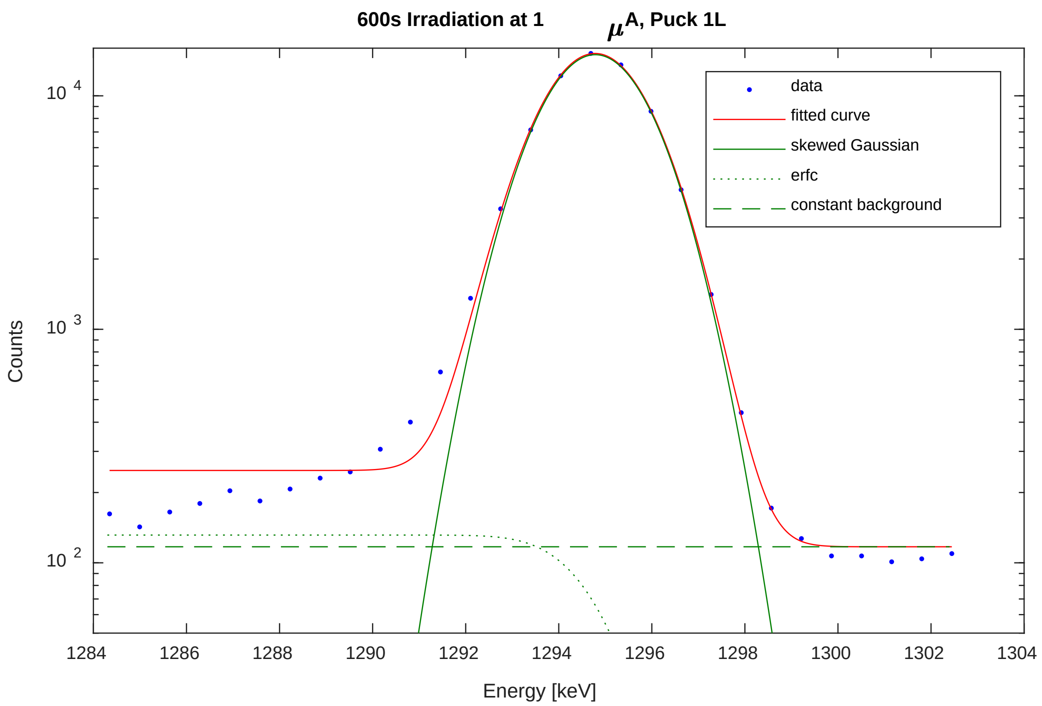

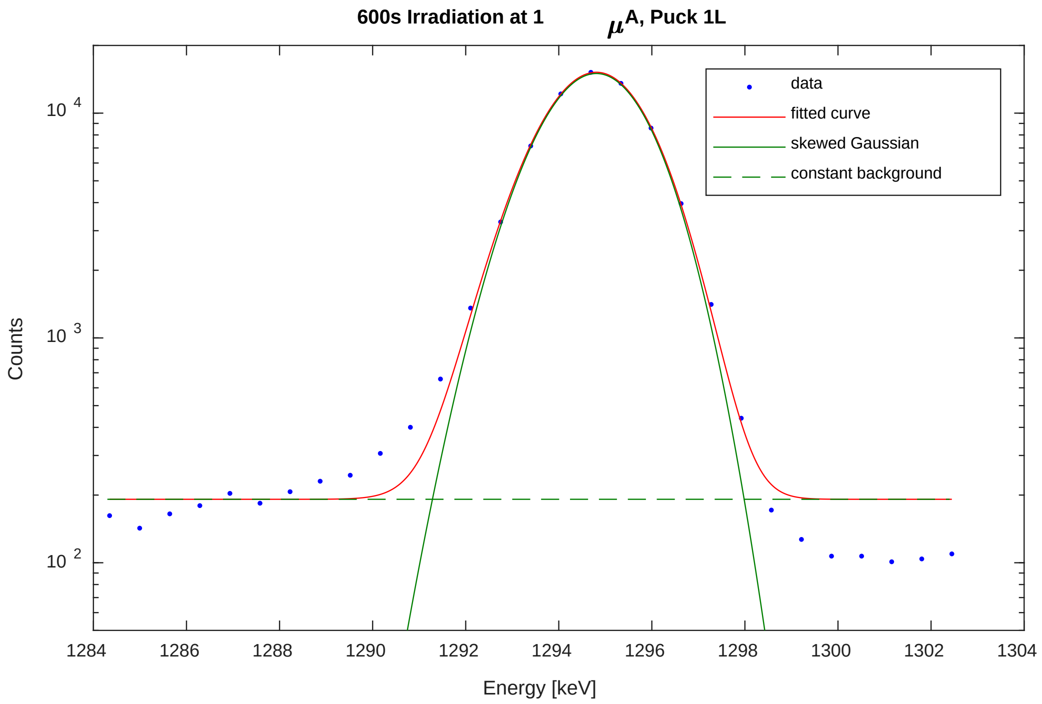

Figure 13: Contributions to a sample fitted curve by different components within each fit displayed on a logarithmic scale. The fit with three terms and seven free parameters follows the background more closely, but that advantage is removed if the characteristic

width of the skewed Gaussian is fixed. Seven free parameters were deemed to be excessive, and the two-term fit follows the data more closely with five free parameters than does the three-term fit with fixed characteristic widths.

The net counts inside the skewed Gaussian out to a width of $\pm 2\sigma$ were integrated for the signal, while the background was the area under the constant D. Because both the signal (C) and the background (B) follow Poisson processes, their errors are $\sqrt{C}$ and $\sqrt{B}$, and the cumulative (sum of squares) statistical error is $\sqrt{C+B}$. To include the error resulting from the fits, upper bounds for each of the constants were calculated, and the maximum peak, widths, and background were integrated over the maximum width out to $\pm 2\sigma$. The square root of the gross counts under this maximal-area peak was then used as the error, and it included both statistical and fitting uncertainties.

The next adjustment to be applied to the data was a dead-time correction. For the MURR data, dead times approached 20% in the beginning of the readout period for the pucks that were nearest to the source, and so a correction needed to be applied. The correction applied was identical to that used in Knoll [6], and to the first order is the same for both paralyzable and non-paralyzable detectors. It states that the actual number of events is equal to the measured number of events divided by the quantity 1 minus the ratio of dead time to real time. The Mercury data had dead times of approximately 1%, but the correction was applied for the sake of consistency.

The MURR data were then combined with the modeled neutron flux provided by the MURR staff (table 2), puck mass, integration time, and time constants similar to equation 6 to get F-factors for each peak, substituting the modeled flux for $Y/4\pi d^2 t_0$. Different calibration factors from shots with bare pucks at 10.2, 22.9, and 35.6 cm are compared in figure 14. Because the MCNP simulation of the MURR spectrum was the most detailed for the 10 cm position, the F-factor for each peak in that position was used to calibrate the F-factors for the Mercury source.

Distance	Flux (neutrons/cm^{2}s)
10.2 cm	1.56 x 10^8
22.9 cm	1.30 x 10^8
35.6 cm	6.16 x 10^7

Table 2: Energy-integrated neutron flux at different locations from the target.

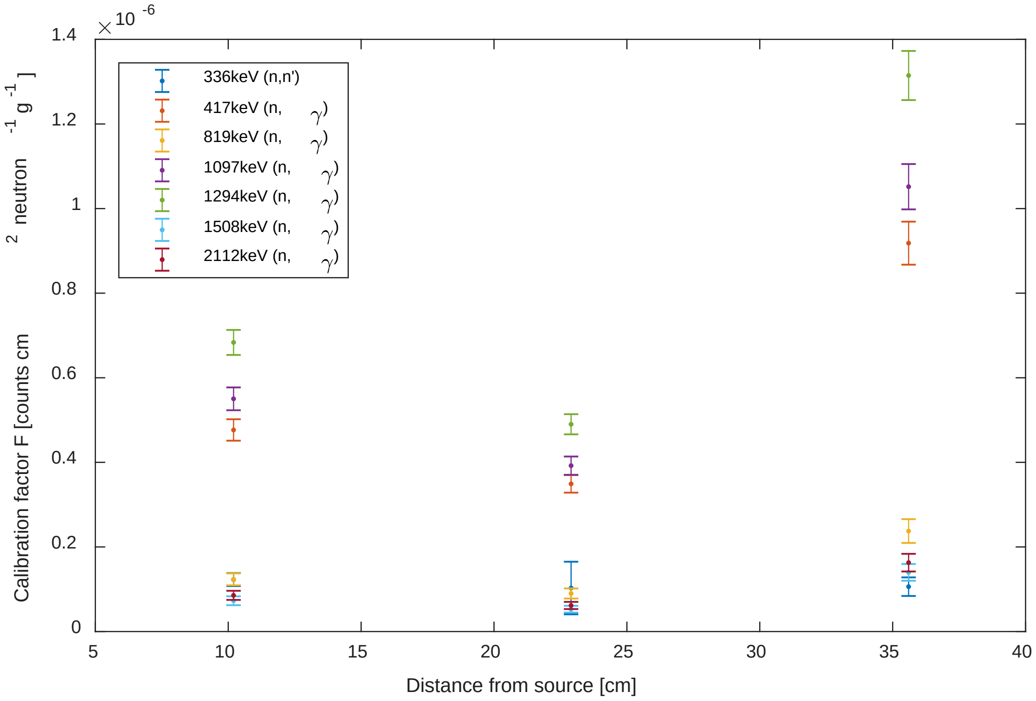

Figure 14: F-factors vs. distance. The calculated F-factors at MURR for each fitted peak at each distance are displayed. Error bars at one standard deviation have been multiplied by 10 for visibility. Variation in the calibration factors may stem from incorrect flux models at each location, or from variation in scatter background.

The F-factors carry a dependence on spectral characteristics of the beam, because the detection efficiency ε_D depends on the capture cross section of the neutrons as shown in figure 1. To correct for this spectral dependence, the energy-integrated flux from both sources was set to 1, and then the source energy spectra were multiplied by the cross sections for the n,γ reaction, as shown in figure 15. The MCNP simulation of the Mercury spectrum contained hundreds of tiny bins, while the MURR simulation contained between ten and twenty bins. Because of this, and because of the difference in source intensity, the number of neutrons in each bin in the MURR simulation was much larger than the number of neutrons per bin in the Mercury simulation. Re-binning the source simulations would either lose information on the Mercury spectrum, or artificially create false information about the MURR spectrum, so they were simply plotted with different y-axes. The convolved spectra were integrated with respect to energy, and the proportion of the results is the ratio by which the MURR F-factors were multiplied to get F-factors for the Mercury spectrum.

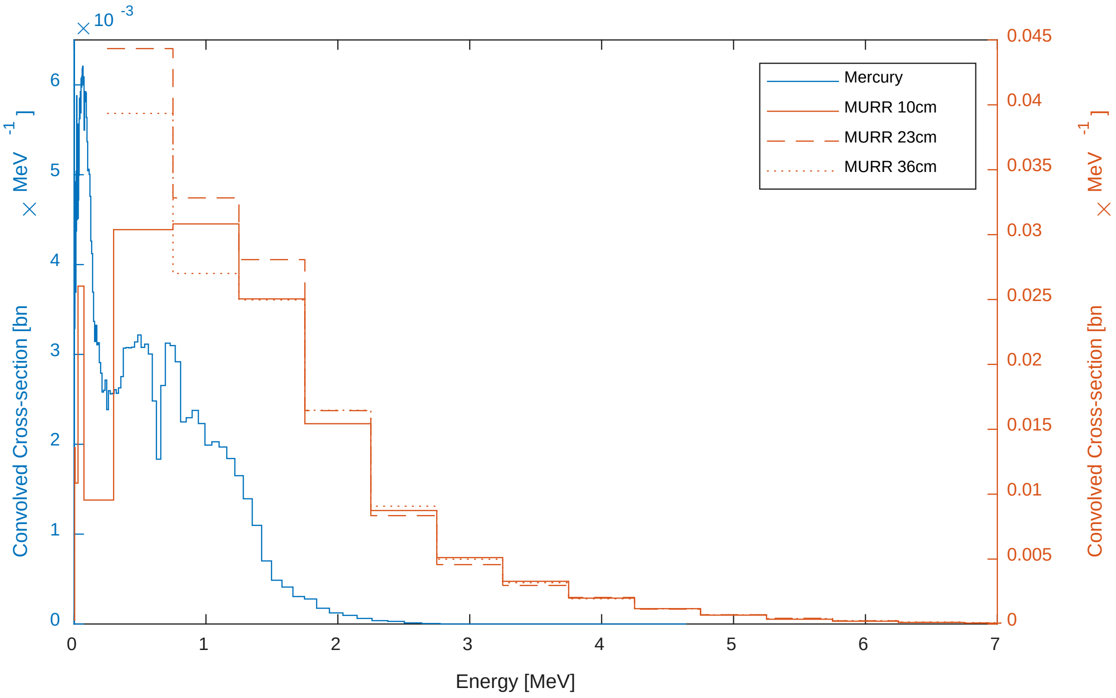

Figure 15: Mercury and MURR spectra convolved with the cross section of ^{115}*In(n,γ)* ^{116m}*In. The y-axes appear differently due to nonuniform binning in MCNP.*

For the n,n′ reaction, the Mercury and MURR spectra were truncated below the cutoff of 339.2 keV before normalization. This meant that the calculated F-factors reflect only the neutron yield above 339.2 with no contribution from thermal neutrons. Without this extra step, the calibration factor was highly sensitive to any errors in the MCNP models of the Mercury and MURR source spectra, because only 30.4% of the Mercury spectrum and 79.6% of the MURR spectrum are above the cutoff. Cross sections and calibration factors for Mercury and MURR are displayed in .

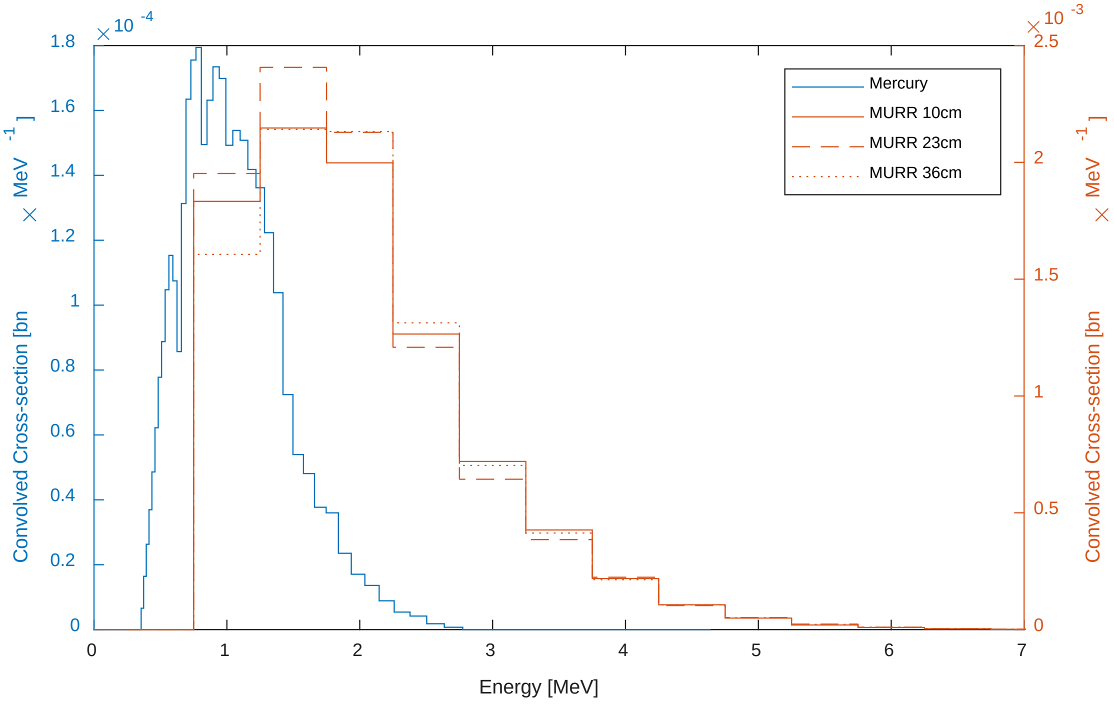

Figure 16: Mercury and MURR spectra convolved with the cross section of ^{115}In (n,n′) ^{115m}In. The y-axes appear differently due to nonuniform binning in MCNP.

Calibration factor F (keV)	MURR 10 cm	Mercury
336 (n,n′)	1.029e-07±6.2e-09	4.696e-08±5.9e-10
417 (n,γ)	3.491e-07±2.1e-09	4.201e-06±2.2e-08
819 (n,γ)	8.998e-08±1.2e-09	1.088e-06±1.3e-08
1097 (n,γ)	3.922e-07±2.2e-09	4.850e-06±2.4e-08
1294 (n,γ)	4.901e-07±2.4e-09	6.025e-06±2.6e-08

1508 (n,γ)	5.283e-08±8.1e-10	6.418e-07±9.3e-09
2112 (n,γ)	6.163e-08±8.5e-10	7.540e-07±9.5e-09

Table 3: Calibration factors for Mercury and MURR. Uncertainties reflect statistical and fitting uncertainties from calibration data taken at MURR. Because the signal levels at MURR were very high, the error stemming from uncertainties in the fitting parameters was dwarfed by the statistical uncertainty.

The detector F-factor for the beryllium detector data had been calibrated at IBL in 2015. The new calibration factor was calculated in a similar manner as for the n,n′ F-factor, where the downscattered Mercury spectrum was truncated at the cutoff (667 keV for this reaction), multiplied by the cross section of ^{9}Be(n,α)^{6}He and integrated. The result was compared to the same procedure at the IBL spectrum, which was monoenergetic at 2.45 MeV. Counts were taken using a photomultiplier tube and summed between 0.1 and 3 s, with the signal from an empty shot subtracted from each shot containing the sphere, core, or shell. Statistical errors were propagated through the empty shot subtraction, and a weighted average was taken to acquire the final average dose from each target.

The NRL spectra were processed in the same manner as the MURR spectra, but using calibration factors to calculate yield instead of vice versa. Yield was calculated using eq. 8, combining the counts under the peak and counts in background with the start and stop times of the measurement, and distance from the source to calculate expected yield into 4π steradians. The empty shots were subtracted for the n,α reactions to eliminate background. The γ,γ′ reaction in ^{115}In can lead to the same excited state and decay peak as the n,n′ reaction; therefore, empty shots were also subtracted from the n,n′ signal. Unfortunately, the statistical and fitting errors of the 336 keV peak stemming from the n,n′ or γ,γ′ reaction were so large that none of the yields were statistically different from zero after subtraction from the empty shots. Their error bars far exceeded the maximum yields calculated using the n,γ reaction, hence the n,n′ data are not included in the figures. Results in the default configuration with the activation detector positioned three centimeters above the top of the beryllium sphere are displayed in figure 17. The n,γ reaction data reflects the total neutron yield, including thermal background, while the n,α data from the beryllium rod detector reflect only the neutrons above 667 keV in energy.

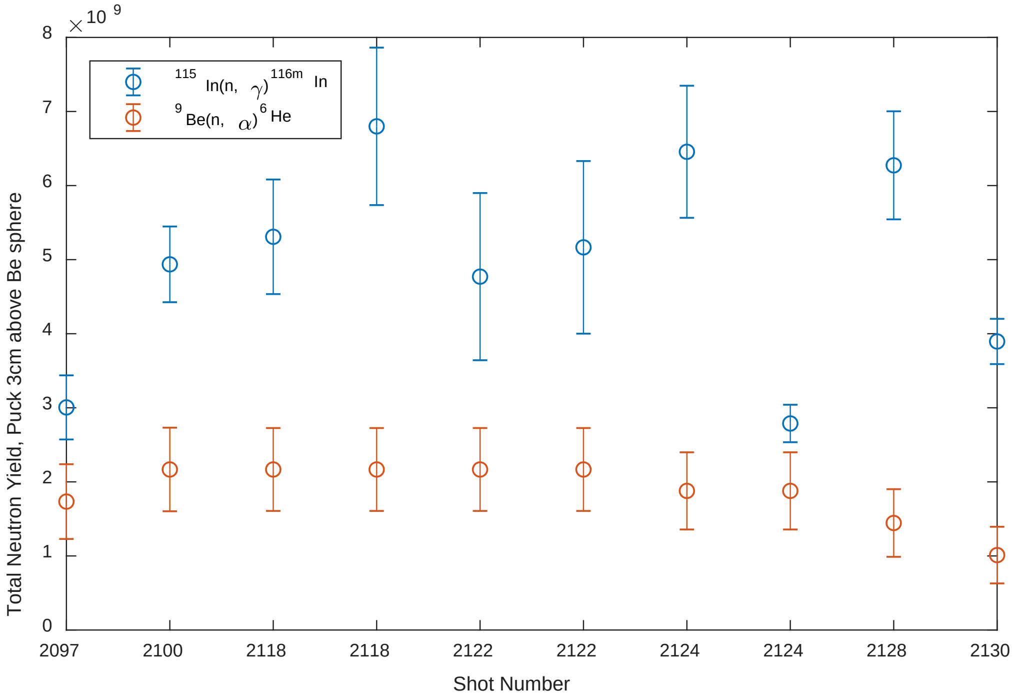

Figure 17: Shot-to-shot variation in yield from the beryllium sphere. Shots with the same number reflect variation in calculated yield from the same puck at different times after irradiation. The standard deviation of the measured yield on all beryllium sphere shots divided by the mean yield gave an estimated variation of 20% using the beryllium detector data.

Different targets were used to test the neutron yield from each component of the beryllium sphere. The sphere consisted of a core and a shell, which were both tested independently. The mean yield from the core was 3.07±0.24E09 neutrons, the shell 2.42±0.33E09 neutrons, and the sphere 3.81±0.15E09 neutrons. The fact that the yields from the core and the shell added together are greater than the yield from the sphere in its entirety (within experimental uncertainty) indicate that the beryllium target sphere is partially self-shielding and that neutrons generated in its core cannot pass through the shell unperturbed. This was anticipated in the MCNP simulations that calculated a different result for the as-born versus the downscattered spectra. Results are shown in figure 18.

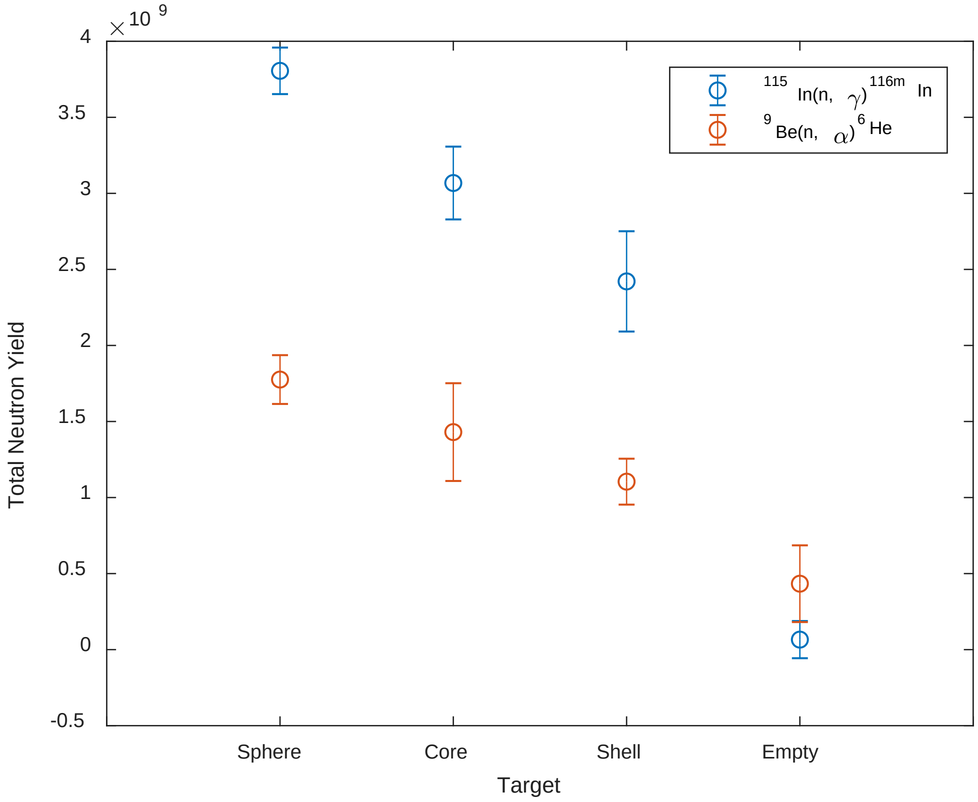

Figure 18. Mean yield from different targets. The sphere consisted of the core encased in the shell. Non-zero yield in empty shots may occur from stray x-rays activating the

beryllium in the detector itself, or also from a very small number of neutrons produced by the machine.

Indium pucks were placed in different orientations with respect to the beryllium sphere to examine the thermal neutron background in different locations. As expected, the yield below the sphere measured by the n,γ reaction was much higher due to the presence of large amounts of steel in close proximity. When the puck was in the horizontal plane of the sphere, it was farther from the steel table and stage, leading to a decreased thermal background, and when placed above the sphere, the background decreased further (figure 19). Results are plotted in figure 19.

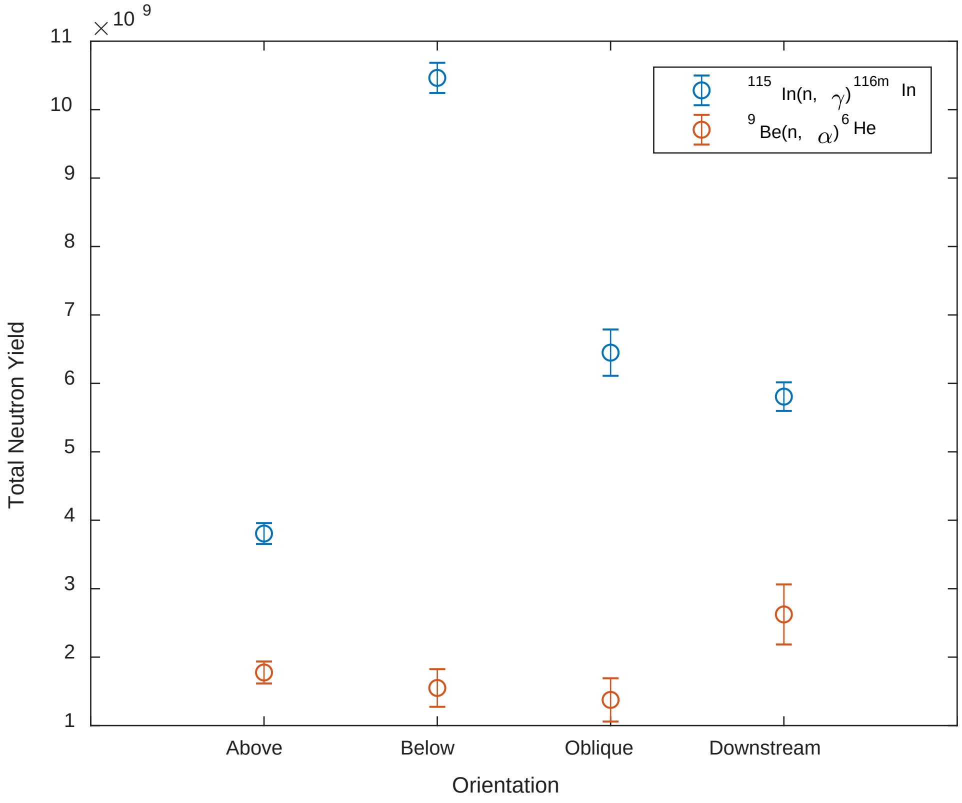

Figure 19: Effect of position with respect to the beryllium sphere on measured yield. Higher thermal neutron backgrounds occur below the sphere due to proximity to scatter

sources; farther from the sphere, the background will be higher relative to the signal, leading to an increased yield measurement. The position of the beryllium rod detector used in the n,α measurement remained stationary during the data run, but is used to eliminate the possibility of the source producing more neutrons for the handful of shots that were taken with indium pucks positioned below, downstream, or oblique to the photoneutron source.

To further estimate the contribution of the thermal neutron background, the yield measured by pucks placed at different distances from the beryllium sphere was examined. The pucks were held in place at an identical height over the steel table in an effort to keep the scatter background similar at each location. Corrections for distance were made, as usual, using a $1/r^2$ dependence. While not entirely perfect in the near-field limit, the calculated difference is miniscule at distances greater than 1.5 times the radius of the ball away from the center of the sphere, which was the closest distance examined. Unfortunately, as the distance from the sphere was increased, the number of counts decreased sufficiently to produce large statistical and fitting errors, so this method of estimating the yield produced by scatter background was inconclusive.

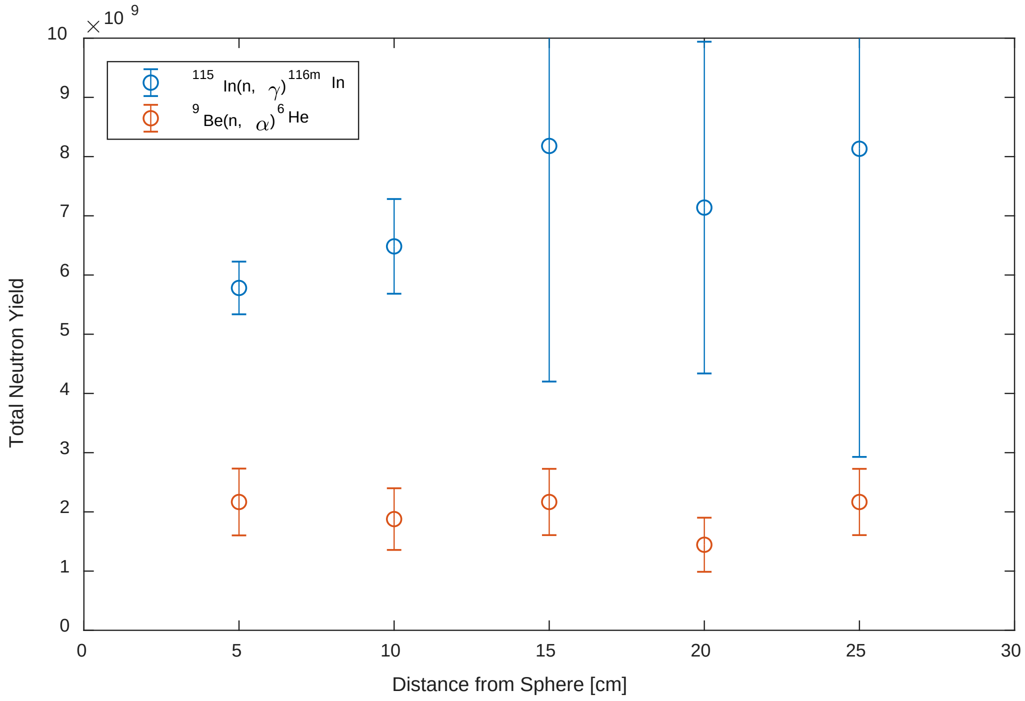

Figure 20: Total neutron yield as measured by indium pucks placed at different distances from the sphere placed in the same horizontal plane. As the pucks are positioned farther from the sphere and they see fewer counts, large statistical and fitting uncertainties occur.

The yield from the n,α reaction was used to measure the yield of neutrons above the cutoff energy of 667 keV, which was 1.78±0.16E09 neutrons according to a weighted average. It is possible to use the full Mercury spectrum to estimate the total yield if the yield above 667 keV is known, but the uncertainties in the low-energy part of the spectrum are sufficiently high to render such a measurement indeterminate. The best way to measure the thermal background would be to place an indium puck very far away from the source and integrate the signal for a sufficiently long time to build up statistics. Barring that, more accurate MCNP modeling could help determine exactly how much of the downscattered spectrum should be above and below the 667 keV cutoff.

Conclusion

The total neutron yield of a pulsed source with 5 MeV endpoint was measured using indium and beryllium activation detectors. These detectors were sensitive to neutron yields produced by targets of different mass and different scatter backgrounds. They were reasonably simple to calibrate using the F-factor method. It was determined that the total photoneutron yield from the beryllium source was 3.81±0.15 neutrons including the scatter background and 1.78±0.16 neutrons with energy above 667 keV. The shot-to-shot variation of the source was estimated to be 20%.

Activation detectors are small, mechanically robust, and well-suited for experimental environments with high electromagnetic interference. These diagnostics required some averaging to handle low count levels and estimates for thermal backgrounds to which the detectors were sensitive, but were otherwise straightforward to use.

Future work may include studying different materials such as silver or gold to better match the neutron spectrum for the photoneutrons created by the Mercury pulsed-power source. The use of additional HPGe detectors to read out more detectors concurrently to improve statistical uncertainties and directly measure the neutron scatter background should also be considered.

Acknowledgments

This manuscript has been authored with support by Mission Support and Test Services, LLC, under Contract No. DE-NA0003624, with the U.S. Department of Energy, National Nuclear Security Administration, Office of Defense Programs. The United States Government retains and the publisher, by accepting the article for publication, acknowledges that the United States Government retains a non-exclusive, paid-up, irrevocable, worldwide license to publish or reproduce the published form of this manuscript, or allow others to do so, for United States Government purposes. The U.S. Department of Energy will provide public access to these results of federally sponsored research in accordance with the DOE Public Access Plan (http://energy.gov/downloads/doe-public-access-plan). The views expressed herein do not necessarily represent the views of the U.S. Department of Energy or the United States Government.

DOE/NV/03624--0171

References

[1] Zier, J. C., et al., “High-power, photofission-inducing bremsstrahlung source for intense pulsed active detection of fissile material.” *Physical Review Special Topics-Accelerators and Beams* 17.6 (2014): 060401.

[2] D.A. Brown, M.B. Chadwick, R. Capote, et al., “ENDF/B-VIII.0: The 8th Major Release of the Nuclear Reaction Data Library with CIELO-project Cross Sections, New Standards and Thermal Scattering Data,” Nuclear Data Sheets, 148: pp. 1-142 (2018).

[3] ESNDF

[4] Cooper, Gary W., and Carlos L. Ruiz. “NIF total neutron yield diagnostic.” *Review of Scientific Instruments* 72.1 (2001): 814-817.

[5] Ruiz, C. L., et al. “Absolute calibration of a total yield indium activation detector for DD and DT neutrons.” *Review of Scientific Instruments* 63.10 (1992): 4889-4891.

[6] Knoll, Glenn F. *Radiation Detection and Measurement*. John Wiley & Sons, 2010.

[7] Hughes, R. J., et al., “The photoneutron cross section of ^{9}Be.” *Nuclear Physics A* 238.2 (1975): 189-198.

[8] Goldemberg, J., and L. Katz. “High energy gamma-gamma cross section of In^{115}.” *Physical Review* 90.2 (1953): 308.

[9] Gilmore, Gordon. *Practical Gamma-Ray Spectroscopy*. John Wiley & Sons, 2011.

[10] Bevington, Philip R., and D. K. Robinson. *Data Reduction and Error Analysis for the Sciences*. McGraw-Hill, 1992, 172-174.

[11] Arnold, C. W., et al. “Cross-section measurement of ^{9}Be (γ, n) ^{8}Be and implications for $\alpha + \alpha + n \rightarrow {}^{9}$Be in the r process.” *Physical Review C* 85.4 (2012): 044605.